Nanoscale

PAPER

View Article Online
View Journal | View Issue

Cite this: *Nanoscale*, 2025, **17**, 9222

Structural diversity dependent cation incorporation into magnetic Cr–Se nanocrystals†

Yifen Wang,‡[a] Wei Zhao,‡[a] Bin Wang,[a] Zhendong Song,[a] Huan Yang,[a] Fang Wang,[a] Xiaohong Xu[a] and Yang Liu*[b]

Chromium selenide (Cr–Se)-based low-dimensional materials have attracted significant attention in spintronics because of their diverse structure- and composition-dependent magnetic properties. While significant progress has been made in fabricating the Cr–Se family of nanomaterials through techniques like chemical vapor deposition, the synthesis of Cr–Se nanocrystals (NCs) *via* colloidal methods remains underexplored. In this work, we demonstrate the robust colloidal synthesis approach for producing Cr_2Se_3 and Cr_3Se_4 NCs with distinct morphologies by varying the Cr precursors and ligands. Cr–Se NCs can serve as templates for cation exchange (CE) reactions involving monovalent Cu^+ and Ag^+, divalent Zn^{2+} and Cd^{2+}, and trivalent In^{3+}, facilitating the creation of a diverse library of metal selenide NCs and nanoheterostructures. Our findings highlight how the outcomes of CE reactions are influenced by the structure of various Cr–Se phases. Furthermore, the magnetic properties of the as-synthesized Cr–Se NCs and their derivative $CuCrSe_2$ were investigated. Our work provides a robust synthesis route for the Cr–Se class of magnetic nanomaterials and a platform for creating a diverse range of functional metal selenide NCs *via* CE reactions.

Received 30th November 2024,
Accepted 12th March 2025

DOI: 10.1039/d4nr05035e

rsc.li/nanoscale

Introduction

The Cr–Se family of materials has garnered significant attention in the exploration of two-dimensional magnets due to their high Curie temperatures and air-stability, providing opportunities to investigate a wide range of magnetic properties in the 2D realm. Various stable and metastable stoichiometries within the Cr–Se material class, such as CrSe,[1] Cr_2Se_3,[2] Cr_3Se_4,[2] Cr_5Se_8,[3] Cr_9Se_{13},[4] and $CrSe_2$,[5,6] have been synthesized. For instance, He's group demonstrated the presence of noticeable ferromagnetic properties in 2D CrSe crystals grown *via* chemical vapor deposition (CVD) at temperatures below 280 K.[1] In another study, Duan *et al.* grew air-stable $CrSe_2$ nanosheets on WSe_2 substrates using a CVD approach, showcasing ferromagnetic behavior.[5] Despite the predominance of previous research on Cr–Se nanomaterials relying on CVD and exfoliation techniques, which suffer from low productivity, hindering large-scale practical applications, colloidal synthesis emerges as a promising method for crafting 2D materials with a tailored morphology, thickness, and composition.[7,8] More importantly, it enables the production of freestanding 2D materials amenable for doping *via* the chemical method[9] and integration into thin-film devices through solution processing.[10,11] Despite the recent progress in colloidal Cr-based NCs,[12–16] to the best of our knowledge, the colloidal synthesis of Cr–Se NCs remains unexplored.

In colloidal synthesis, the CE reaction, which describes the scenario that the cations in the host lattice are replaced by

[a]*Research Institute of Materials Science of Shanxi Normal University & Key Laboratory of Magnetic Molecules and Magnetic Information Materials of Ministry of Education, Taiyuan 030031, China*
[b]*Department of Materials Science, Fudan University, Shanghai 200433, China. E-mail: liuyang_fd@fudan.edu.cn*

†Electronic supplementary information (ESI) available. See DOI: https://doi.org/10.1039/d4nr05035e

‡These authors contributed equally to this work.

Yang Liu

Yang Liu is an associate professor at the Department of Materials Science, Fudan University. He received his Ph.D. in Chemical Engineering from the State University of New York (SUNY) at Buffalo in 2018. From 2018 to 2021, he was a Postdoctoral Research Fellow in the Department of Chemistry at Indiana University Bloomington. His research focuses on the synthesis and applications of novel metal chalcogenide nanomaterials for electrocatalysis and energy storage devices, as well as the discovery of novel magnetic two-dimensional materials.

foreign cations without largely modifying the anionic sublattice, presents a distinctive avenue for generating a diverse array of metal chalcogenide NC libraries.[17,18] The copper chalcogenide class of nanomaterials, *i.e.*, $Cu_{2-x}S$, $Cu_{2-x}Se$, and $Cu_{2-x}Te$ with $0 \leq x \leq 1$, serves as the robust template for CE reactions due to the varied crystal structures and morphologies achievable through colloidal synthesis.[19,20] Furthermore, the Cu^+ ions in the degenerately doped structure possess fluid-like ion mobility at elevated temperature.[21] In the metal selenide regime, CdSe NCs can serve as the template for CE with Cu^+ to produce Cu_2Se and $Cu_{2-x}Se$ NCs.[22] Besides these advancements, there is a need for additional metal selenide templates with a tunable morphology and crystal structures for not only understanding the mechanism of CE reactions on metal selenides, but also fostering the development of previously unprecedented metal selenide-based nanostructures.

In this work, we demonstrate that Cr–Se NCs can serve as templates for CE reactions, facilitating the creation of a diverse range of metal selenide NCs. By employing $Cr(acac)_3$ or $CrCl_2$ precursors, we synthesised Cr–Se NCs with varying crystal structures and morphologies, resulting in the production of distinct Cr_2Se_3 and Cr_3Se_4 NCs. The subsequent CE reactions with monovalent Cu^+ and Ag^+, as well as trivalent In^{3+}, led to distinct reaction products when using the two Cr–Se templates, while the outcomes were similar when divalent Zn^{2+} and Cd^{2+} were applied. For example, ultrathin InSe nanosheets with lateral dimensions exceeding a micron can be synthesized *via* In^{3+} exchange with Cr_2Se_3 nanoplatelets. The valence selectivity of CE reactions originated from the structural disparities between more symmetric Cr_2Se_3 unit cells and lattice-disordered Cr_3Se_4. Additionally, we investigated the magnetic properties of Cr–Se NCs and their derivative $CuCrSe_2$. Our work provides valuable insights into the relationship between structural dependent cation incorporation and magnetic properties of Cr–Se based low-dimensional nanomaterials.

Experimental

Chemicals

Oleylamine (OAm, 80–90%) and cadmium(II) chloride ($CdCl_2$, 99.99%) were purchased from Aladdin. Trioctylphosphine (TOP, 97%), chromium(III) acetylacetonate ($Cr(acac)_3$, 97%), copper(II) acetylacetonate ($Cu(acac)_2$, 97%), zinc(II) chloride ($ZnCl_2$, ≥98%), hexamethyldisilazane (HMDS, 99.9%) and oleic acid (OA, 90%) were purchased from Sigma-Aldrich. Tri-*n*-octylamine (TOA, 97%) was purchased from TCI Chemicals. Chromium(II) chloride ($CrCl_2$, 99.99%), chromium(0) hexacarbonyl ($Cr(CO)_6$, 99%), selenium (Se, 99.999%, 200 mesh), and indium(III) chloride ($InCl_3$, 99.99%) were purchased from Alfa Aesar. Silver(I) acetate (Ag(OAc), 99%) was purchased from Adamas-beta. All chemicals were used as received.

Synthesis of Cr–Se NCs

All NC syntheses were carried out using standard Schlenk techniques under a nitrogen atmosphere. The detailed synthetic parameters and product NCs are provided in Table S1.† In a typical synthesis of Cr–Se NCs, 1.0 mmol $CrCl_2$, 1 mL OA, 1 mL HMDS, and 6 mL of TOA were loaded into a three-neck flask. Under a nitrogen flow, the mixture was maintained at room temperature for 30 min and then heated at 100 °C for another 30 min to form a clear solution. In a separate vial, the TOP–Se precursor was prepared by dissolving 2.0 mmol of Se powder into 2.0 mL of TOP *via* stirring in a nitrogen-filled glove box at 100 °C. The reaction mixture was heated to 300 °C before injection of the TOP–Se precursor. The reaction was kept at the reaction temperature for 3 hours before being air-cooled to room temperature. The Cr–Se NCs were isolated by 10 mL ethanol precipitation and centrifugation at 4000 rpm for 5 min. The NCs were redispersed in 10 mL of hexane and precipitated with 10 ml of ethanol before being centrifuged at 4000 rpm for 3 min. After another cycle of precipitation and centrifugation, Cr–Se NCs were dissolved in hexane for further use. The synthesis of Cr–Se nanoplatelets and nanoflowers follows the same synthetic procedure except for using different metal precursors, ligands, and synthetic parameters.

CE reaction with Cr–Se NCs

The detailed synthetic parameters and product NCs are provided in Table S2.† In a typical synthesis of InSe nanosheets, 0.05 mmol $InCl_3$ and 6 mL OAm were loaded into a three-neck flask. Under a nitrogen flow, the mixture was maintained at room temperature for 30 min and then heated at 100 °C for another 30 min to form a clear solution. In a separate vial, Cr–Se nanoplatelet solution was prepared by dissolving 13.1 mg dry Cr–Se nanoplatelets into 3.0 mL OAm and 1.0 mL TOP by sonication. After injection of the Cr–Se solution, the reaction mixture was heated to 340 °C and kept at this temperature for 2 hours before being air-cooled to room temperature. The InSe nanosheets were isolated by 10 mL ethanol precipitation and centrifugation at 4000 rpm for 5 min. The nanosheets were redispersed in 10 mL of hexane and precipitated with 10 ml of ethanol before being centrifuged at 4000 rpm for 3 min. After another cycle of precipitation and centrifugation, InSe nanosheets were dissolved in hexane for further use. The synthesis of InSe nanosheets using Cr–Se nanoplates and nanoflowers follows the same synthetic procedure except for using different synthetic parameters.

Characterization

Transmission electron microscopy (TEM) images, high-resolution TEM (HRTEM) images, and STEM-energy-dispersive X-ray spectroscopy (STEM-EDS) maps were obtained with a JEM-F200 operating at an accelerating voltage of 200 kV. TEM grids were prepared by placing a dilute NC dispersion onto a carbon-coated copper grid and allowing the sample to air dry. Powder X-ray diffraction (XRD) measurements were performed using a Rigaku Ultima IV diffractometer equipped with a Cu Kα X-ray source. Samples were prepared by drop-casting concentrated NC dispersions onto glass slides. X-ray photoelectron spectroscopy (XPS) spectra were acquired using an ESCALAB 250Xi with an Al Kα X-ray source (1486.6 eV) and a nominal spot diameter of 400 μm. The analysis chamber pressure was maintained below 5×10^{-8}

mbar. Magnetic hysteresis (*M–H*) loops, along with field-cooling (FC) and zero-field cooling (ZFC) curves, were measured using a Physical Property Measurement System (PPMS).

Results and discussion

We synthesized Cr–Se NCs with different crystal structures and morphologies *via* a colloidal method. In general, the Se precursor was introduced into the Cr precursor complex *via* a hot-injection approach. When $Cr(acac)_3$ was used as the Cr precursor, the synthesis yielded small nanoplatelets, with an average diameter of 13.2 ± 0.1 nm, as demonstrated by the TEM image in Fig. 1a. Size distribution histograms for this and the following samples are provided in Fig. S1 and S9.† The STEM-EDS elemental maps (Fig. 1b) demonstrate uniform distribution of Cr and Se signals across the nanoplatelets with a Cr : Se ratio of 42.6% : 57.4%, indicating the presence of Se vacancies. The corresponding EDS spectra and quantitative results of the elemental maps in this work are collectively provided in Fig. S2–S3 and Table S3.† The XRD pattern and selective area electron diffraction (SAED) pattern (Fig. 1c and d) suggest the formation of the Cr_2Se_3 phase, with diffraction peaks/rings that correspond to the (002), (116), and (300) planes within the Cr_2Se_3 unit cell. As shown in Fig. 1e, the XPS spectrum in the Cr 2p region reveals the peaks at 587.0 eV and 577.2 eV, suggesting that Cr is exclusively present as Cr^{3+}. The peaks observed in the XPS spectrum in the Se 3d region correspond to Se^{2-} (Fig. S4a†). The XPS results matched well with the previous observations on Cr_2Se_3.[2,23]

In contrast, the synthesis of Cr–Se NCs involving the $CrCl_2$ precursor led to the formation of Cr_3Se_4 NCs with a larger size in nanoplate and nanoflower morphologies, featuring the average size of 45.5 ± 0.2 nm and 444.0 ± 6.6 nm, respectively, with TOA and OAm ligands (Fig. 1f and k, and Fig. S1†). The STEM-EDS elemental maps illustrate the co-localization of Cr and Se signals on the individual nanoplate and nanoflower with Cr : Se ratios of 43.1% : 56.9% and 43.2% : 56.8%, respectively (Fig. 1g and l), consistent with their XRD patterns that matched well with the Cr_3Se_4 phase (Fig. 1h and m). Note that the Cr_2Se_3 nanoplatelets and Cr_3Se_4 nanoplates exhibited varying full width at half maxima (FWHM) in XRD peaks, reflecting differences in crystalline size and anisotropy. Furthermore, the HRTEM images reveal an observed lattice spacing of 5.9 Å on the side-view of the nanoplate, corresponding to the (002) planes in the Cr_3Se_4 unit cell (Fig. 1i), highlighting that the basal planes of the nanoplates are (002) planes in Cr_3Se_4. The XPS spectra of Cr (Fig. 1j and o) and Se (Fig. S4b and c†) for nanoplates and nanoflowers indicated that Cr is present as a mixture of Cr^{2+} and Cr^{3+}, while Se is present as Se^{2-}, consistent with a previously report on Cr_3Se_4.[2] The formation of the plate-like morphology is attributed to the layered atomic arrangement of the unit cell (Fig. S5†), as supported by the side-view HRTEM image. A similar lattice structure was observed on the nanoflowers, indicating that the nanoflowers were composed of assembled nanoplates (Fig. 1n). Ligand-assisted phase engineering and morphology engineering have been employed as powerful tools for creating diverse NCs with a controlled morphology, composition and crystal structure.[12,24] TOA, considered a weakly coordinating

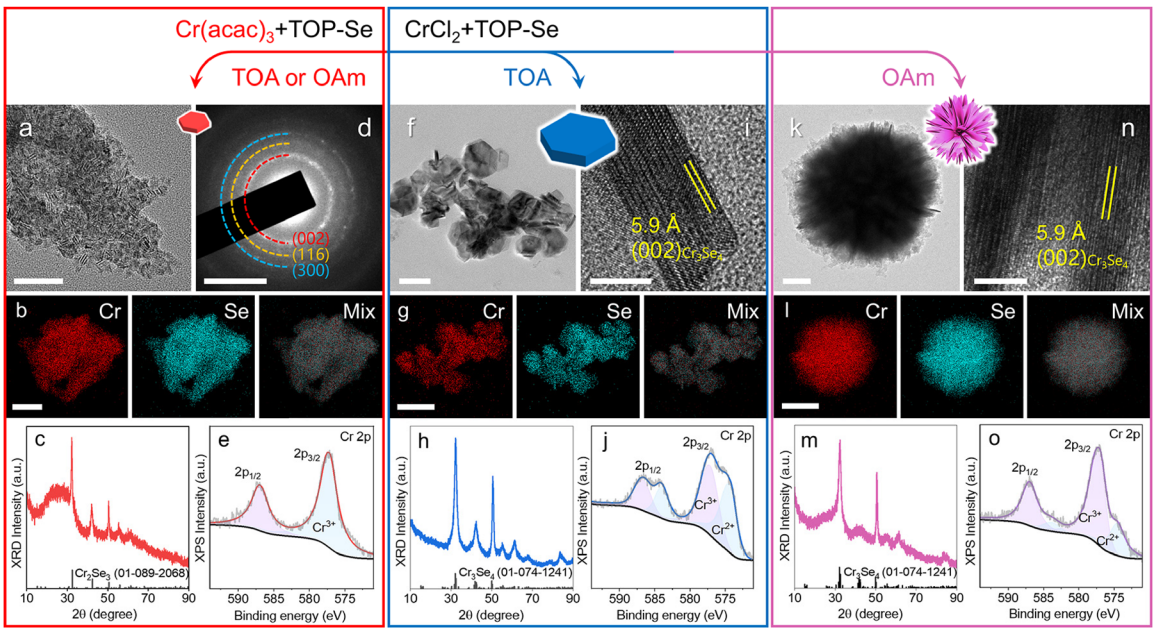

Fig. 1 Synthesis of Cr–Se NCs. (a) TEM image, (b) STEM-EDS elemental maps of Cr and Se, (c) XRD pattern, (d) SAED pattern, and (e) XPS spectrum of Cr for Cr_2Se_3 nanoplatelets. (f) TEM image, (g) STEM-EDS elemental maps of Cr and Se, (h) XRD pattern, (i) HRTEM image, and (j) XPS spectrum of Cr for Cr_3Se_4 nanoplates. (k) TEM image, (l) STEM-EDS elemental maps of Cr and Se, (m) XRD pattern, (n) HRTEM image, and (o) XPS spectrum of Cr for Cr_3Se_4 nanoflowers. Scale bars: (a) 50 nm, (b, g and l) 200 nm, (f and k) 100 nm, (i and n) 5 nm, and (d) 5 nm^{-1}.

ligand compared to OAm due to its larger steric bulk and lower ligand surface packing, likely contributes to a more disordered and thicker ligand shell during nanoplate growth, preventing the formation of the assembled nanoplate architectures. Compared with small nanoplatelets, the formation of nanoplates and nanoflowers can be attributed to the utilization of an inorganic Cr precursor ($CrCl_2$), whose reactivity is higher than that of $Cr(acac)_3$. This can be also supported by the increased Cr : Se ratio from the stoichiometry between two phases and the increased size of the NCs. Furthermore, the synthesis of Cr–Se NCs using $Cr(CO)_6$ leads to the formation of Cr_2Se_3 NCs, regardless of the ligands (OAm or TOA) involved in the reaction (Fig. S6†). The obtained NCs exhibited a nanoplatelet morphology, indicating that the $Cr(CO)_6$ precursor may exhibit a similar reactivity to $Cr(acac)_3$.

CE reactions have emerged as a versatile method for tailoring the composition and crystal structure of metal selenide NCs.[17,25,26] A template with diverse crystal structures and morphologies is pivotal for expanding the range of accessible metal selenide nanostructures. While copper selenide templates have commonly been used in CE reactions to synthesize a diverse range of metal selenide NCs, we demonstrate that the Cr–Se NCs can also serve as templates during CE reactions. We first explored the CE reactions on Cr–Se NCs with In^{3+}. The In–Se class of materials is known for their unique properties such as a large band gap, high mobility, and highly anisotropic electrical and thermal properties, making them promising for applications in optoelectronics, thermoelectric devices and photocatalysis.[27–30] The controlled syntheses in the previous reports yielded distinct In–Se phases in either InSe[29] or In_2Se_3,[28] while the CE reaction with Cr–Se NCs in our work led to the formation of both phases, depending on the Cr–Se template used and the injection temperature. As shown in Fig. 2a, at an injection temperature of 300 °C, monodisperse

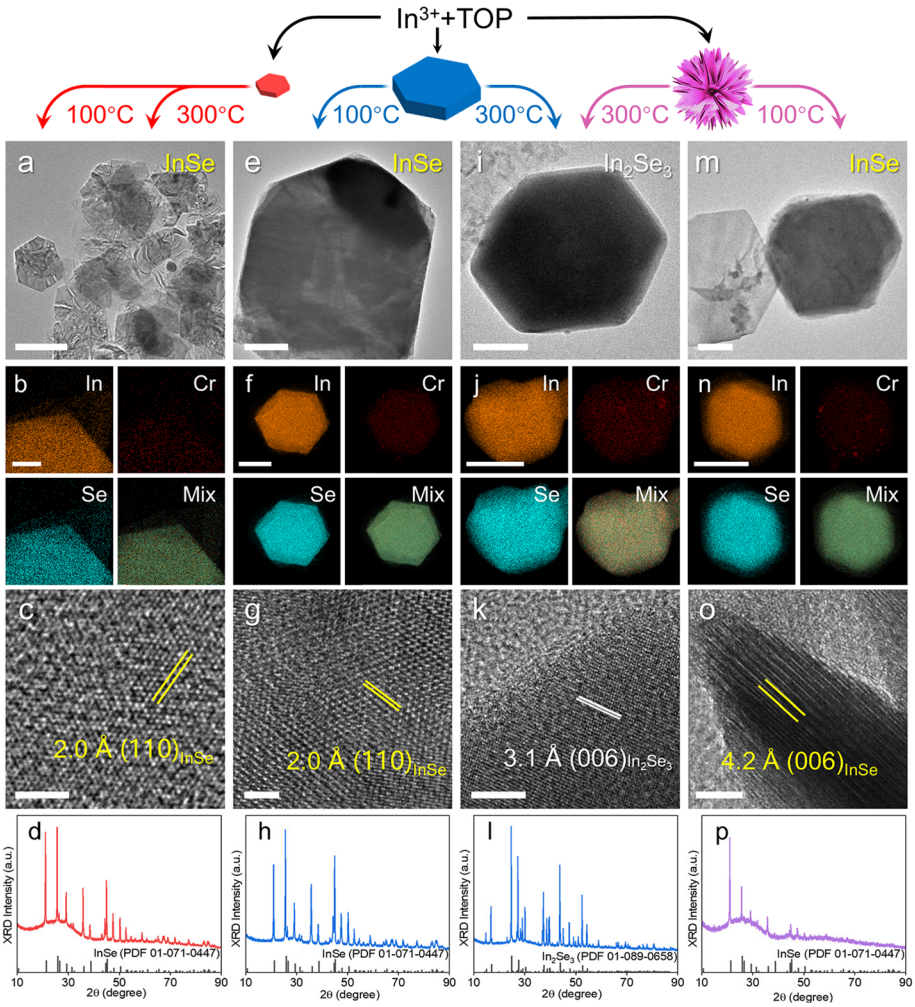

Fig. 2 Synthesis of In–Se nanosheets *via* CE reactions. TEM image, STEM-EDS elemental maps of In, Cr and Se, HRTEM image, XRD pattern of (a–d) InSe nanosheets obtained using In^{3+} exchange with Cr_2Se_3 nanoplatelets at 300 °C. (e–h) InSe nanosheets obtained using In^{3+} exchange with Cr_3Se_4 nanoplates at 100 °C and (i–l) In_2Se_3 nanosheets obtained using In^{3+} exchange with Cr_3Se_4 nanoplates at 300 °C. (m–p) InSe nanosheets obtained using In^{3+} exchange with Cr_3Se_4 nanoflowers at 100 °C. Scale bars: (a, e and f) 1 μm, (c and g) 2 nm, (k and o) 5 nm, (b and i) 100 nm, (j and n) 500 nm, and (m) 200 nm.

nanosheets with a lateral size approaching a micron can be produced *via* CE reactions employing small Cr_2Se_3 nanoplatelet templates. The formation of larger nanosheets using ~13 nm nanoplatelets suggested a ripening process occurring *via* the merging of smaller nanoplatelets during the CE reaction. STEM-EDS elemental maps (Fig. 2b) confirmed the uniformly distributed In and Se signals with an expected ~1 : 1 In : Se ratio, along with minimal residual Cr signal presence. The side-view HRTEM image in Fig. 2c shows the lattice spacing of 2.0 Å, corresponding to the (110) planes in InSe from XRD analysis (Fig. 2d). Similar InSe nanosheets were obtained by injecting Cr_2Se_3 nanoplatelets into an In-complex solution at 100 °C (Fig. S7†), indicating the negligible impact of injection temperature on the selective synthesis of In–Se compounds when using Cr_2Se_3 templates.

When the CE of In^{3+} was performed with Cr_3Se_4 nanoplates and nanoflowers at 100 °C, comparable nanosheets were produced (Fig. 2e and m). The formation of the InSe phase was validated by the XRD patterns (Fig. 2h and p), the observed lattice spacings 2.0 Å and 4.2 Å for the (110) and (006) planes (Fig. 2g and o), and the homogeneously distributed In and Se signals in STEM-EDS elemental maps (Fig. 2f and n). In contrast to the use of small Cr_2Se_3 templates, elevating the injection temperature with Cr_3Se_4 nanoplates resulted in In_2Se_3 nanosheets, as evidenced by the TEM image, HRTEM image, STEM-EDS elemental maps, and XRD patterns (Fig. 2i–l). Similarly, employing Cr_3Se_4 nanoflowers as templates in CE reactions yielded predominantly the In_2Se_3 phase, with a minor presence of InSe as a secondary phase (Fig. S8†). As shown in Fig. S9,† the results demonstrate that InSe nanosheets synthesized *via* CE reactions on Cr_3Se_4 nanoplates exhibit the largest lateral dimensions and thickness (3.8 μm and 68.6 nm, respectively) compared to those grown on Cr_2Se_3 nanoplatelets and Cr_3Se_4 nanoflowers. This observation can be attributed to the highly faceted morphology of Cr_3Se_4 nanoplates, which contrasts with the less defined structures of the other Cr–Se templates. The CE reaction, which is strongly dependent on cation diffusion, proceeds more efficiently on the well-defined facets of anisotropic NCs. In contrast, Cr_2Se_3 nanoplatelets and Cr_3Se_4 nanoflowers require significant morphological evolution to form large, faceted InSe nanosheets. Furthermore, In_2Se_3 nanosheets are generally smaller but thicker than InSe nanosheets, a difference that can be explained by the non-layered structure of the In_2Se_3 unit cell compared to the van der Waals structure of InSe (Fig. S10†).

Furthermore, the general CE reactions with Cr–Se NCs can be extended to various cations including Cu^+, Ag^+, Zn^{2+}, and Cd^{2+} (Fig. 3a). Fig. 3c1 shows a typical TEM image of the products obtained *via* the CE of Cu^+ on small Cr_2Se_3 nanoplatelets, revealing a lattice spacing of 2.0 Å corresponding to the (220) planes of Cu_2Se (Fig. 3c2). The XRD pattern and the STEM-EDS elemental maps further confirm the formation of the Cu_2Se nanoparticles (Fig. 3b and c3), with the Cr content largely removed, indicating a tendency for Cu^+ ions to completely replace the Cr^{3+} ions within the Cr_2Se_3 lattice. By contrast, the CE reactions of Cu^+ on Cr_3Se_4 nanoplates and nanoflowers lead to the ternary $CuCrSe_2$ phase, retaining the morphology of the respective templates (Fig. 3d1 and e1). The formation of the ternary $CuCrSe_2$ phase is confirmed by the XRD patterns and HRTEM images (Fig. 3b, d2, and e2). This indicates the potential of CE reactions in synthesizing 2D magnets in addition to conventional methods like CVD.[31–33] The STEM-EDS elemental maps confirmed the colocation of Cu, Cr, and Se with an atomic ratio of 24.6% : 27.4% : 48.0% and 26.4% : 23.5% : 50.2% (Fig. 3d3 and e3). These observations suggest that Cu^+ ions tended to coexist with Cr^{3+} in the Cr_3Se_4 lattice, further highlighting the significant influence of the crystal phase and morphology on the outcomes of CE reactions.

The CE reactions of Ag^+ on Cr–Se NCs yielded results akin to those obtained with Cu^+. The reaction on Cr_3Se_4 nanoplates and nanoflowers produced Cr_3Se_4–Ag_2Se heterostructures (Fig. 3f), suggesting that Ag^+ partially occupied the surface of Cr_3Se_4 NCs, followed by regioselective CE reactions (Fig. 3h1 and i1). The formation of these heterostructures was confirmed by the HRTEM image and separate signals of Cr and Ag (Fig. 3h2, h3 and i2, i3) as well as the clear heterointerface along the two domains in the HRTEM image (Fig. 3g1 and g2). In contrast, CE reactions on the small Cr_2Se_3 nanoplatelets resulted in more complete reactions, forming Cr_2Se_3–Ag_2Se–Ag heterostructures, with the remaining Cr signals less pronounced compared to the Ag signals (Fig. 3g3). Notably, the lattice fringes were obviously different in the two areas of a single nanoparticle, consistent with our previous observation that the excess Ag^+ could deposit on the Ag_2S surface as Ag metallic nanoparticles when the CE reaction was complete.[34]

The CE reactions of divalent Zn^{2+} and Cd^{2+} with Cr–Se NCs follow a similar trend, producing ZnSe and CdSe NCs, respectively, as demonstrated by the XRD patterns and homogeneous distribution of Zn/Cd and Se signals across the entire NCs (Fig. 3j–q). Generally, the morphologies of the products were preserved from the particle, plate, and flower templates, with the size of the products obtained with Cd^{2+} being consistently larger than those with Zn^{2+} (Fig. S1†). This size difference arises from the larger ionic radius of Cd^{2+} (78 pm) compared to Zn^{2+} (60 pm), leading to lattice expansion during the CE process. This is supported by the observed larger lattice spacing in the HRTEM images, 3.3 Å for ZnSe (Fig. 3m2) and 3.7 Å for CdSe (Fig. 3q2).

The above observations highlight the significant role of the crystal structure in dictating the outcomes of CE reactions. The products obtained by the CE reaction involving monovalent cations (Cu^+ and Ag^+) and the trivalent cation (In^{3+}) on Cr_2Se_3 nanoplatelets are generally different from those obtained with Cr_3Se_4 nanoplates and nanoflowers, while similar results are observed when divalent cations (Zn^{2+} and Cd^{2+}) are used. We speculate that the discrepancy originated from the structural difference between Cr_2Se_3 and Cr_3Se_4 during CE reactions. The Cr_2Se_3 unit cell comprises a hexagonal lattice, while Cr_3Se_4 adopts a monoclinic structure. In the Cr_3Se_4 unit cell, there are two types of Cr cations (Cr^{2+} and Cr^{3+}) with the coexistence of both ordered and disordered octa-

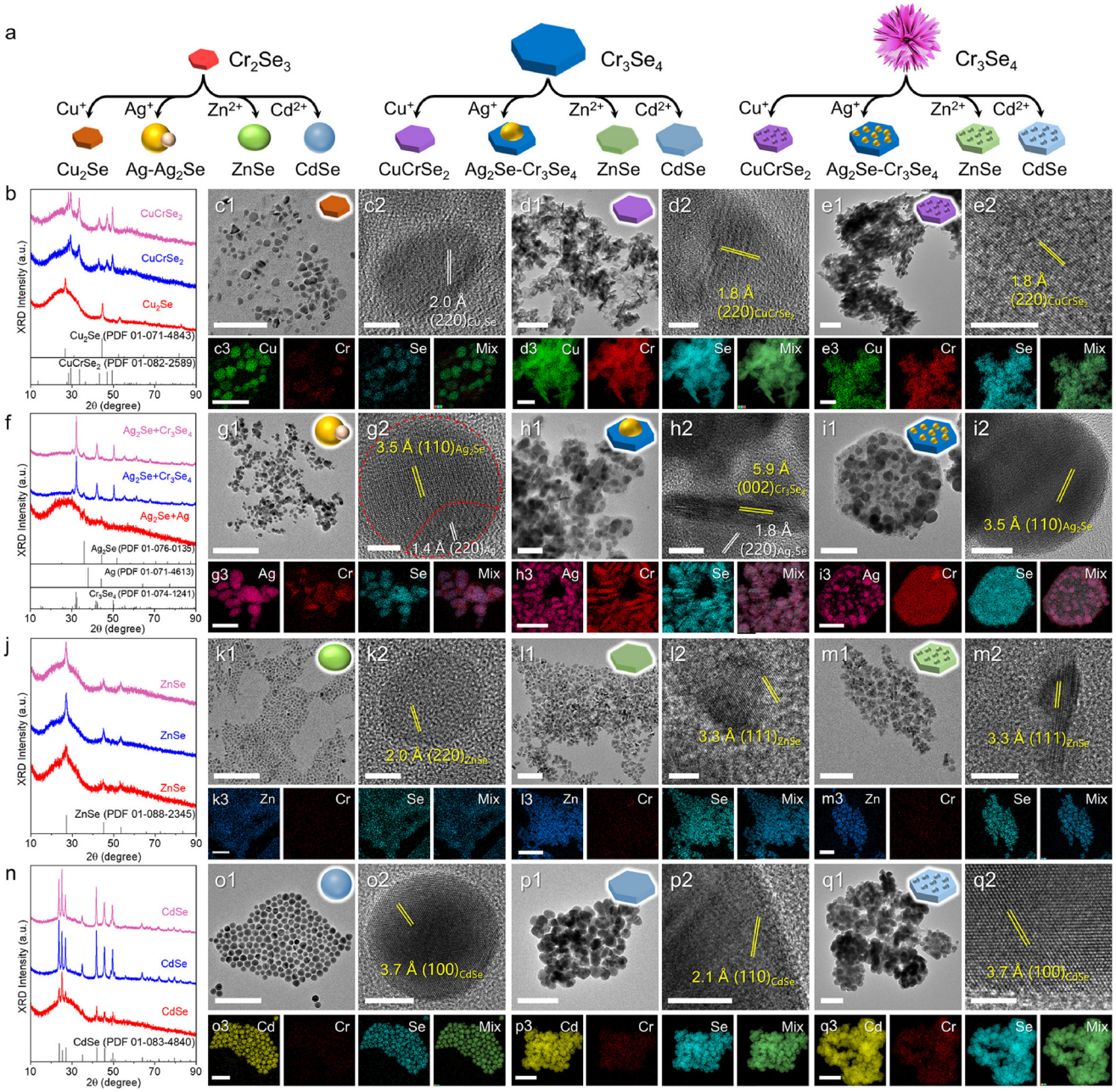

Fig. 3 CE reactions with Cu^+, Zn^{2+}, Ag^+, and Cd^{2+}. (a) Schematic illustration of the valence-dependent CE reaction on Cr–Se templates. (b) XRD patterns of Cu^+ exchange with Cr–Se NCs. TEM image, STEM-EDS elemental maps, and HRTEM image of Cu^+ exchange with (c) Cr_2Se_3 nanoplatelets, (d) Cr_3Se_4 nanoplates, and (e) Cr_3Se_4 nanoflowers. (f) XRD patterns of Ag^+ exchange with Cr–Se NCs. TEM image, STEM-EDS elemental maps, and HRTEM image of Ag^+ exchange with (g) Cr_2Se_3 nanoplatelets, (h) Cr_3Se_4 nanoplates, and (i) Cr_3Se_4 nanoflowers. (j) XRD patterns of Zn^{2+} exchange with Cr–Se NCs. TEM image, STEM-EDS elemental maps, and HRTEM image of Zn^{2+} exchange with (k) Cr_2Se_3 nanoplatelets, (l) Cr_3Se_4 nanoplates, and (m) Cr_3Se_4 nanoflowers. (n) XRD patterns of Cd^{2+} exchange with Cr–Se NCs. TEM image, STEM-EDS elemental maps, and HRTEM image of Cd^{2+} exchange with (o) Cr_2Se_3 nanoplatelets, (p) Cr_3Se_4 nanoplates, and (q) Cr_3Se_4 nanoflowers. Scale bars: (c1, l1, m1, i1, m3, h3, i3, k3, l3 and o3) 100 nm, (d1, e1, g1, k1, o1, p1, q1, e3, p3 and q3) 200 nm, (c3, d3, g3 and h1) 50 nm, (m2, h2, o2 and p2) 10 nm, and (c2, d2, e2, g2, i2, l2, k2 and q2) 5 nm.

hedron-coordinated centers, leading to a higher degree of lattice disorder in Cr_3Se_4. These features allow the Cr_3Se_4 structure to provide more available sites for incoming cations to replace, potentially lowering the energy barrier for Cr ions to coexist with incoming cations, thereby fostering greater structural diversity in the products post-CE reactions. Furthermore, the coexistence of Cr^{3+} and Cu^+ in the $CuCrSe_2$ unit cell, the stoichiometrically decreased In : Se ratio in In_2Se_3 with a disordered lattice (Fig. S10†), and the predominant formation of the Cr_3Se_4–Ag_2Se heterostructures after CE reactions

on Cr_3Se_4 indicate a tendency towards relatively incomplete CE processes. By contrast, the more symmetric Cr_2Se_3 unit cell facilitates more complete CE reactions, forming Cu_2Se, InSe, and Ag_2Se–Ag heterostructures when Cu^+, In^{3+} and Ag^+ ions are used, respectively. For divalent cations, the CE reactions produced binary ZnSe and CdSe indiscriminatingly, as other stoichiometric Zn–Se or Cd–Se phases may not be stabilized under ambient conditions. These results underscore that CE reactions can be used to identify the crystal phase and structures of the templates.[35–37]

For In exchange, when Cr_2Se_3 nanoplatelets were used as a template, the reaction yielded InSe nanosheets. InSe exhibits promising physical properties including higher carrier mobilities and thickness-dependent bandgaps, which enhance its potential for application in field-effect transistors (FETs) with high on/off current ratios at room temperature.[38–40] In contrast, when Cr_3Se_4 nanoplates and nanoflowers were used as templates for cation exchange, both InSe and In_2Se_3 nanosheets were obtained. In_2Se_3 has become one of the leading candidates for visible photodetection, owing to its narrow bandgap, direct bandgap characteristics, high absorption coefficient within the visible spectrum, and exceptional sensitivity.[28,41–43] These results highlight the potential of the template in regulating the properties of cation exchange products. For monovalent Cu^+ exchange, the complete cation exchange product Cu_2Se, which was obtained using the Cr_2Se_3 template, features a p-type semiconductor with a tunable bandgap (1.1–1.5 eV) and a direct bandgap (2.0–2.3 eV). These characteristics allow Cu_2Se to play significant roles in energy conversion and storage applications, including solar cells, lithium-ion batteries, supercapacitors, and thermoelectric devices.[44–46] By contrast, the incorporation of Cu into Cr_3Se_4 leads to the formation of $CuCrSe_2$ NCs, which exhibit antiferromagnetism. Very recently, multiferroicity has been observed in thin layer $CuCrSe_2$,[32,33] highlighting the influence of the template on the properties of products after cation exchange reactions. Ag_2Se is a typical n-type thermoelectric material near room temperature with high carrier mobility and low thermal conductivity.[47,48] Integration with metallic Ag nanoparticles has the potential to enhance the thermoelectric performance of the Ag_2Se domain by improving electron transfer. ZnSe and CdSe are well-known for their applications in light-emitting diodes (LEDs) and optoelectronic devices.[49,50] Although their crystal phase and stoichiometry are difficult to tune *via* the choice of Cr–Se templates for cation exchange, the resulting ZnSe and CdSe NCs inherit the size and morphology of their Cr–Se templates. The size- and structure-dependent optical and electronic properties allow for diverse applications.

The metal selenide NCs discussed above hold significant potential for a wide array of applications, such as catalysis, energy storage, and optoelectronics. As a proof-of-concept demonstration, we aimed to leverage the magnetic properties of Cr_2Se_3, Cr_3Se_4, and $CuCrSe_2$. These colloidal Cr–Se-based nanomaterials offer two immediate advantages. Firstly, the colloidal approach provides a pathway for the scalable synthesis of magnetic materials for solution-processed thin film devices, with carrier mobility comparable to bulk materials achievable through ligand exchange and annealing processes. Secondly, these NCs with their standalone nature hold promise as templates for incorporating foreign cations/anions to alter magnetic ordering or enhance the Curie temperature. To explore these advantages, the magnetic properties of the synthesized Cr–Se and $CuCrSe_2$ NCs with different morphologies were investigated by PPMS measurements. Fig. 4a and b display the hysteresis loops and ZFC and FC magnetization results for Cr_2Se_3 nanoplatelets, indicating a ferromagnetic behavior with a T_C of ~80 K and exhibiting paramagnetic ordering at higher temperature, consistent with the previous reports.[2,51,52] Compared to Cr_2Se_3, the Cr_3Se_4 nanoplates displayed a slightly lower T_C of ~50 K but a higher coercivity (Fig. 4c and d). The

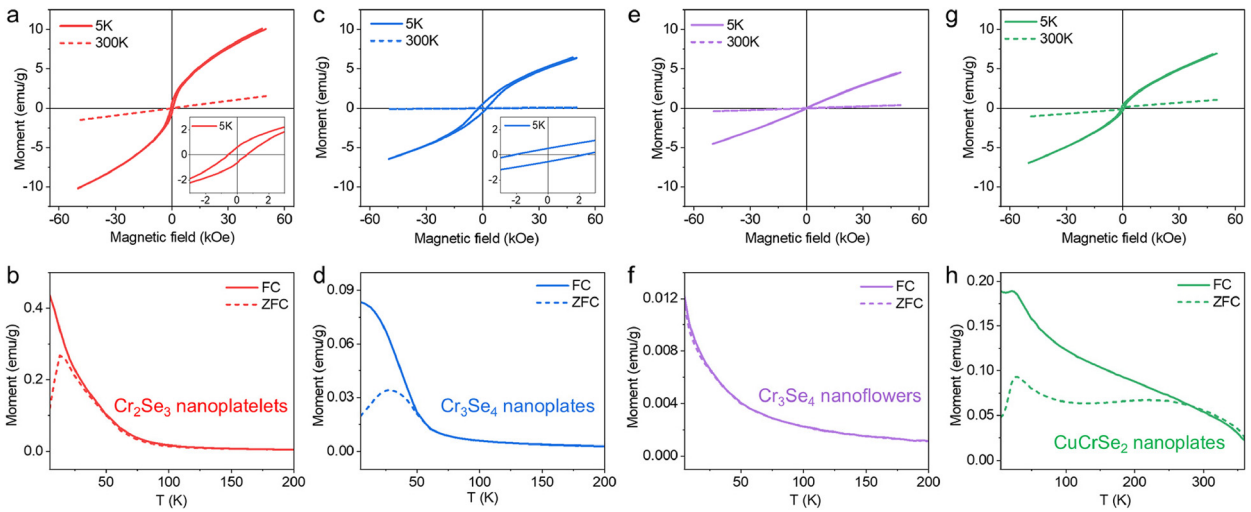

Fig. 4 Magnetic measurements of Cr–Se and $CuCrSe_2$ NCs. *M*–*H* and *M*–*T* curves of (a and b) Cr_2Se_3 nanoplatelets, (c and d) Cr_3Se_4 nanoplates, (e and f) Cr_3Se_4 nanoflowers, and (g and h) $CuCrSe_2$ nanoplates obtained through CE with Cr_3Se_4 nanoplates.

magnetic behavior is different from the recently reported Cr_3Se_4 flakes, possibly due to the size effect of the sample in this work.[2] In single-domain particles, coercivity increases with size due to magnetic anisotropy scaling with volume. However, multi-domain transitions at larger sizes reduce coercivity *via* domain wall-mediated reversal.[53–55] Cr_3Se_4 nanoplates likely remain single-domain, favoring coherent magnetization reversal, while smaller Cr_2Se_3 may approach pseudo-single-domain states with lower energy barriers for switching. Surface pinning also dominates coercivity in nanostructures. Cr_3Se_4's nanoplate geometry (high aspect ratio, distinct facets) enhances surface anisotropy, stabilizing moments against reversal. In contrast, Cr_2Se_3's compact platelets exhibit weaker pinning, reducing coercivity. This is consistent with the previous reports that shape-dependent surface anisotropy aligns with studies on anisotropic NCs.[56] Moreover, Cr_3Se_4's monoclinic structure likely hosts stronger magnetocrystalline anisotropy than trigonal Cr_2Se_3, amplified by stoichiometry-driven exchange interactions.

For Cr_3Se_4 nanoflowers, the linear relationship in *M–H* loops at both room and low temperatures (Fig. 4e) as well as almost zero coercivity revealed their paramagnetic nature. The pronounced increase in magnetization at low temperatures can be elucidated by dipolar interactions prevailing over thermal energy, thereby promoting moment alignment and consequently augmenting magnetization (Fig. 4f). The discrepancies may arise from the distinct exchange interactions that lead to long-range magnetic order,[2] potentially attributed to the uniformity in sample thickness and the presence of defects during synthesis. While Cr_3Se_4 exhibits paramagnetic ordering overall, the ZFC/FC splitting in nanoplates (~50 K) *versus* overlapping curves in nanoflowers stems from morphology-dependent spin dynamics. In nanoplates, the large planar geometry enhances surface spin density and disorder.[57] At low temperatures, these surface spins experience frustration due to competing interactions,[58] leading to a glass-like state that manifests by the irreversibility in ZFC/FC. Conversely, nanoflowers' 3D branched structure promotes stronger interparticle coupling, which suppresses surface spin effects and stabilizes faster spin relaxation, resulting in reversible paramagnetic behavior.[59] The magnetic properties of Cr–Se NCs are intricately linked to the valence states of Cr cations and their corresponding electron spin configurations.[60] In Cr_2Se_3 and Cr_3Se_4, the valence states of Cr cations (Cr^{2+}, Cr^{3+}) play a critical role in determining spin–orbit coupling, which influences the magnetic ordering. Specifically, Cr^{3+} (d^3 configuration) typically exhibits a high-spin state, favoring ferromagnetic coupling *via* superexchange/double-exchange interactions.[2] In contrast, Cr^{2+} (d^4 configuration) can exhibit varying spin states depending on the crystal field splitting, which may lead to complex magnetic behaviors such as antiferromagnetism or spin-glass states.[51,61] In our study, the observed ferromagnetic behavior in Cr_2Se_3 nanoplatelets (T_C ~ 80 K) and Cr_3Se_4 nanoplates (T_C ~ 50 K) can be attributed to the dominance of Cr^{3+} cations, which promotes strong ferromagnetic coupling. The higher coercivity in Cr_3Se_4 nanoplates compared to Cr_2Se_3 suggests enhanced spin alignment and magnetic anisotropy, likely due to differences in the Cr^{2+}/Cr^{3+} ratio and the resulting electron spin configurations. This is consistent with previous reports that highlight the role of valence states in modulating magnetic properties.[2,61] The paramagnetic nature of Cr_3Se_4 nanoflowers, as evidenced by the linear *M–H* loops and negligible coercivity, further supports the influence of valence states. However, the absence of long-range magnetic order in Cr_3Se_4 nanoflowers may arise from the presence of Cr^{2+} cations, which introduce competing exchange interactions and potential spin frustration.

Upon incorporation with Cu^+, $CuCrSe_2$ exhibited the antiferromagnetic behavior with a Néel temperature (T_N) of ~45 K (Fig. 4g and h), consistent with the previously reported magnetic properties of $CuCrSe_2$.[62,63] This arises from the antiferromagnetically coupled $CrSe_2$ layers between interlayers in $CuCrSe_2$, resulting in an antiferromagnetic ground state. Recent findings indicated the observation of ferromagnetism in $CuCrSe_2$ when the thickness is reduced to a few layers. Work is currently underway to explore the novel magnetic properties of Cr–Se nanoplates with precisely controlled thickness.

Conclusions

In summary, we successfully synthesized a series of colloidal Cr–Se NCs with different crystal phases and morphologies through manipulating the Cr precursor and reaction temperature, producing Cr_2Se_3 nanoplatelets and Cr_3Se_4 nanoplates and nanoflowers. We show that, in addition to the commonly used copper selenide, the Cr–Se class of nanomaterials can serve as the template for the CE reactions to create diverse metal selenide NCs. By reacting the Cr–Se templates with different cations (Cu^+, Ag^+, Zn^{2+}, Cd^{2+}, and In^{3+}), we demonstrated that the outcomes of the CE reactions were strongly influenced by the crystal structure of the templates, which was primarily attributed to the lattice ordering in the Cr–Se template NCs, wherein monodisperse ultrathin InSe nanosheets can be produced. We further explored the magnetic properties of Cr–Se and $CuCrSe_2$ NCs. These findings underscore the significant potential of Cr–Se based NCs in creating novel metal selenide derivatives and exploring their unique properties.

Data availability

The data supporting this article have been included as part of the ESI.†

Conflicts of interest

There are no conflicts to declare.

Acknowledgements

This work was financially supported by the National Key Research and Development Program of China (No. 2024YFB3817400), the National Natural Science Foundation of China (No. 52301298), and the Science and Technology Commission of Shanghai Municipality (No. 22YF1401900).

References

1 Y. Zhang, J. Chu, L. Yin, T. A. Shifa, Z. Cheng, R. Cheng, F. Wang, Y. Wen, X. Zhan, Z. Wang and J. He, *Adv. Mater.*, 2019, **31**, 1900056.
2 F. Cui, K. He, S. Wu, H. Zhang, Y. Lu, Z. Li, J. Hu, S. Pan, L. Zhu, Y. Huan, B. Li, X. Duan, Q. Ji, X. Zhao and Y. Zhang, *ACS Nano*, 2024, **18**, 6276–6285.
3 J. Zhang, Y. Xiao, K. Li, Y. Chen, S. Liu, W. Luo, X. Liu, S. Liu, Y. Wang, S. Y. Li and A. Pan, *Nanoscale*, 2024, **16**, 8028–8035.
4 S. Li, J. Tan, Y. Sun, J. Liu, H. Nong, L. He, Y. Zhang, J. Wang and B. Liu, *Adv. Funct. Mater.*, 2024, **34**, 2403453.
5 B. Li, Z. Wan, C. Wang, P. Chen, B. Huang, X. Cheng, Q. Qian, J. Li, Z. Zhang, G. Sun, B. Zhao, H. Ma, R. Wu, Z. Wei, Y. Liu, L. Liao, Y. Ye, Y. Huang, X. Xu, X. Duan, W. Ji and X. Duan, *Nat. Mater.*, 2021, **20**, 818–825.
6 M. Liu, J. Gou, Z. Liu, Z. Chen, Y. Ye, J. Xu, X. Xu, D. Zhong, G. Eda and A. T. S. Wee, *Nat. Commun.*, 2024, **15**, 1765.
7 M. Nasilowski, B. Mahler, E. Lhuillier, S. Ithurria and B. Dubertret, *Chem. Rev.*, 2016, **116**, 10934–10982.
8 J. H. Han, M. Kwak, Y. Kim and J. Cheon, *Chem. Rev.*, 2018, **118**, 6151–6188.
9 H. Chen, Z. Chen, B. Ge, Z. Chi, H. Chen, H. Wu, C. Cao and X. Duan, *Chem. Mater.*, 2017, **29**, 10019–10026.
10 L. Hu, R. Zhang and Q. Chen, *Nanoscale*, 2014, **6**, 14064–14105.
11 F. Wang and X. Wang, *Nanoscale*, 2014, **6**, 6398–6414.
12 J. Wang, B. Wang, Y. Wang, R. Yang, L. Wang, F. Wang, X. Xu and Y. Liu, *J. Mater. Chem. C*, 2024, **12**, 7725–7731.
13 F. Wang, H. Yang, H. Zhang, J. Zhou, J. Wang, L. Hu, D. J. Xue and X. Xu, *Nano Lett.*, 2021, **21**, 7684–7690.
14 H. Yang, H. Zhang, L. Guo, W. Yang, Y. Wu, J. Wang, X. Li, H. Du, B. Peng, Q. Liu, F. Wang, D. J. Xue and X. Xu, *Nano Lett.*, 2024, **24**, 10519–10526.
15 H. Yang, F. Wang, H. Zhang, L. Guo, L. Hu, L. Wang, D. J. Xue and X. Xu, *J. Am. Chem. Soc.*, 2020, **142**, 4438–4444.
16 Q. Tu, Q. Fu, C. Tang, Y. Xiao, B. Cheng and S. Lei, *Cryst. Growth Des.*, 2022, **22**, 4277–4287.
17 L. T. De and L. Manna, *Chem. Rev.*, 2016, **116**, 10852–10887.
18 C. Coughlan, M. Ibáñez, O. Dobrozhan, A. Singh, A. Cabot and K. M. Ryan, *Chem. Rev.*, 2017, **117**, 5865–6109.
19 Y. Liu, M. Liu and M. T. Swihart, *J. Phys. Chem. C*, 2017, **121**, 13435–13447.
20 M. Liu, Y. Liu, B. Gu, X. Wei, G. Xu, X. Wang, M. T. Swihart and K. T. Yong, *Chem. Soc. Rev.*, 2019, **48**, 4950–4965.
21 T. T. Zhuang, F. J. Fan, M. Gong and S. H. Yu, *Chem. Commun.*, 2012, **48**, 9762–9764.
22 H. Li, M. Zanella, A. Genovese, M. Povia, A. Falqui, C. Giannini and L. Manna, *Nano Lett.*, 2011, **11**, 4964–4970.
23 C. H. Ho and X. R. Lai, *ACS Appl. Electron. Mater.*, 2019, **1**, 370–378.
24 Q. Yun, Y. Ge, B. Huang, Q. Wa and H. Zhang, *Acc. Chem. Res.*, 2023, **56**, 1780–1790.
25 W. Li, R. Zamani, M. Ibáñez, D. Cadavid, A. Shavel, J. R. Morante, J. Arbiol and A. Cabot, *J. Am. Chem. Soc.*, 2013, **135**, 4664–4667.
26 X. Y. Gan, R. Sen and J. E. Millstone, *J. Am. Chem. Soc.*, 2021, **143**, 8137–8144.
27 W. Huang, L. Gan, H. Li, Y. Ma and T. Zhai, *Chem. – Eur. J.*, 2018, **24**, 15678–15684.
28 G. Almeida, S. Dogan, G. Bertoni, C. Giannini, R. Gaspari, S. Perissinotto, R. Krahne, S. Ghosh and L. Manna, *J. Am. Chem. Soc.*, 2017, **139**, 3005–3011.
29 K. H. Park, K. Jang, S. Kim, H. J. Kim and S. U. Son, *J. Am. Chem. Soc.*, 2006, **128**, 14780–14781.
30 J. Lauth, F. E. S. Gorris, M. K. Samadi, T. Chassé, W. Friedrich, V. Lebedeva, A. Meyer, C. Klinke, A. Kornowski, M. Scheele and H. Weller, *Chem. Mater.*, 2016, **28**, 1728–1736.
31 J. Peng, Y. Su, H. Lv, J. Wu, Y. Liu, M. Wang, J. Zhao, Y. Guo, X. Wu, C. Wu and Y. Xie, *Adv. Mater.*, 2023, **35**, 2209365.
32 P. Wang, Y. Zhao, R. Na, W. Dong, J. Duan, Y. Cheng, B. Xu, D. Kong, J. Liu, S. Du, C. Zhao, Y. Yang, L. Lv, Q. Hu, H. Ai, Y. Xiong, V. S. Stolyarov, S. Zheng, Y. Zhou, F. Deng and J. Zhou, *Adv. Mater.*, 2024, **36**, 2400655.
33 Z. Sun, Y. Su, A. Zhi, Z. Gao, X. Han, K. Wu, L. Bao, Y. Huang, Y. Shi, X. Bai, P. Cheng, L. Chen, K. Wu, X. Tian, C. Wu and B. Feng, *Nat. Commun.*, 2024, **15**, 4252.
34 Y. Liu, D. Yin and M. T. Swihart, *Chem. Mater.*, 2018, **30**, 8089–8098.
35 Y. Liu, D. Yin and M. T. Swihart, *Chem. Mater.*, 2018, **30**, 1399–1407.
36 Y. Liu, M. Liu and M. T. Swihart, *J. Am. Chem. Soc.*, 2017, **139**, 18598–18606.
37 Y. Liu, M. Liu, D. Yin, L. Qiao, Z. Fu and M. T. Swihart, *ACS Nano*, 2018, **12**, 7803–7811.
38 W. Feng, W. Zheng, W. Cao and P. Hu, *Adv. Mater.*, 2014, **26**, 6587–6593.
39 S. Sucharitakul, N. J. Goble, U. R. Kumar, R. Sankar, Z. A. Bogorad, F. C. Chou, Y. T. Chen and X. P. A. Gao, *Nano Lett.*, 2015, **15**, 3815–3819.
40 D. A. Bandurin, A. V. Tyurnina, G. L. Yu, A. Mishchenko, V. Zólyomi, S. V. Morozov, R. K. Kumar, R. V. Gorbachev, Z. R. Kudrynskyi, S. Pezzini, Z. D. Kovalyuk, U. Zeitler, K. S. Novoselov, A. Patanè, L. Eaves, I. V. Grigorieva, V. I. Fal'ko, A. K. Geim and Y. Cao, *Nat. Nanotechnol.*, 2017, **12**, 223–227.

41 Z. Q. Zheng, J. D. Yao and G. W. Yang, *J. Mater. Chem. C*, 2016, **4**, 8094–8103.
42 S. Chen, X. Liu, X. Qiao, X. Wan, K. Shehzad, X. Zhang, Y. Xu and X. Fan, *Small*, 2017, **13**, 1604033.
43 W. Feng, W. Zheng, F. Gao, X. Chen, G. Liu, T. Hasan, W. Cao and P. Hu, *Chem. Mater.*, 2016, **28**, 4278–4283.
44 H. Liu, X. Shi, F. Xu, L. Zhang, W. Zhang, L. Chen, Q. Li, C. Uher, T. Day and G. J. Snyder, *Nat. Mater.*, 2012, **11**, 422–425.
45 J. Zhu, Q. Li, L. Bai, Y. Sun, M. Zhou and Y. Xie, *Chem. – Eur. J.*, 2012, **18**, 13213–13221.
46 Y. Su, G. Li, Z. Guo, Y. Y. Li, Y. X. Li, X. J. Huang and J. H. Liu, *ACS Appl. Nano Mater.*, 2018, **1**, 245–253.
47 D. Li, B. L. Zhang, H. W. Ming, L. Wang, Y. Zu and X. Y. Qin, *ACS Appl. Mater. Interfaces*, 2021, **13**, 34543–34549.
48 S. Huang, T. R. Wei, H. Chen, J. Xiao, M. Zhu, K. Zhao and X. Shi, *ACS Appl. Mater. Interfaces*, 2021, **13**, 60192–60199.
49 Y. Wang, Y. Luo, X. Kong, T. Wu, Y. Lin, Z. Chen and S. Wang, *Nanoscale*, 2025, **17**, 1764–1789.
50 W. Zhu, Z. Lin, X. Zhang, W. Wang and Y. Li, *Nanoscale*, 2022, **14**, 11210–11217.
51 S. Luo, X. Zhu, H. Liu, S. Song, Y. Chen, C. Liu, W. Zhou, C. Tang, G. Shao, Y. Jin, J. Guan, V. C. Tung, H. Li, X. Chen, F. Ouyang and S. Liu, *Chem. Mater.*, 2022, **34**, 2342–2351.
52 X. Zhu, H. Liu, L. Liu, L. Ren, W. Li, L. Fang, X. Chen, L. Xie, Y. Jing, J. Chen, S. Liu, F. Ouyang, Y. Zhou and X. Xiong, *Chem. Mater.*, 2021, **33**, 3851–3858.
53 A. G. Kolhatkar, A. C. Jamison, D. Litvinov, R. C. Willson and T. R. Lee, *Int. J. Mol. Sci.*, 2013, **14**, 15977–16009.
54 P. Guardia, A. Labarta and X. Batlle, *J. Phys. Chem. C*, 2011, **115**, 390–396.
55 J. Msomi and T. Moyo, *J. Magn. Magn. Mater.*, 2009, **321**, 1246–1250.
56 Q. Song and Z. J. Zhang, *J. Am. Chem. Soc.*, 2004, **126**, 6164–6168.
57 W. Li, Y. Wang, X. Y. Cui, S. Yu, Y. Li, Y. Hu, M. Zhu, R. Zheng and S. P. Ringer, *ACS Appl. Mater. Interfaces*, 2018, **10**, 19235–19247.
58 R. Fuglsby, P. Kharel, W. Zhang, S. Valloppilly, Y. Huh and D. J. Sellmyer, *J. Appl. Phys.*, 2015, **117**, 17D115.
59 J. Jang, P. K. Srivastava, M. Joe, S. G. Jung, T. Park, Y. Kim and C. Lee, *ACS Nano*, 2025, **19**, 999–1006.
60 L. Lin, P. Su, Y. Han, Y. Xu, Q. Ni, X. Zhang, P. Xiong, Z. Sun, G. Sun and X. Chen, *eScience*, 2025, **5**, 100264.
61 X. Liu, Y. Gebredingle, X. Guo, F. Zhang and N. Kim, *Adv. Funct. Mater.*, 2024, **34**, 2316834.
62 G. C. Tewari, T. S. Tripathi, H. Yamauchi and M. Karppinen, *Mater. Chem. Phys.*, 2014, **145**, 156–161.
63 G. C. Tewari, M. Karppinen and A. K. Rastogi, *J. Solid State Chem.*, 2013, **198**, 108–113.